Article

Study on Transverse Deformation Characteristics of a Shield Tunnel under Earth Pressure by Refined Finite Element Analyses

Wen Long [1], Weijie Chen [2], Changfu Huang [3], Dongyang Li [4] and Dong Su [2,5,6,*]

1   Zhuhai Da Heng Qin City New Center Development Co., Ltd., Zhuhai 519030, China
2   College of Civil and Transportation Engineering, Shenzhen University, Shenzhen 518060, China
3   China Railway 15th Bureau Group Co., Ltd., Shanghai 200070, China
4   Zhuhai Institute of Urban Planning & Design, Zhuhai 519000, China
5   Key Laboratory for Resilient Infrastructures of Coastal Cities (MOE), Shenzhen University, Shenzhen 518060, China
6   Shenzhen Key Laboratory of Green, Efficient and Intelligent Construction of Underground Metro Station, Shenzhen 518060, China
*   Correspondence: sudong@szu.edu.cn; Tel.: +86-0755-2653-5204

Abstract: We establish an elaborate numerical model with which to investigate the deformation characteristics of segmental lining. The numerical model contains reinforcement and connecting bolts that previous numerical studies have generally neglected. We validated the model parameters using a full-scale model test result. Based on this numerical model, we studied the deformation characteristics of segmental lining. Convergence, joint deformation, bolt stress, and reinforcement stress were systematically analyzed under different loading conditions. Furthermore, we discuss the relationships between convergence and joint opening, bolt stress and joint opening. The deformation characteristics of segmental lining are revealed. When the lining is deformed by earth pressure, plastic hinges form at the joints. The segment rotates around the plastic hinge, which is the main reason for segmental lining deformation under earth pressure. Horizontal convergence is a single index to reflect the deformation of tunnel rings, representing the overall deformation of the ring to a certain extent but not the deformation characteristics of the joint. When the loading conditions differ, the relationship between joint opening and horizontal convergence is consistent for some joints and inconsistent for others.

Keywords: shield tunnel; segmental lining; symmetrical structure; numerical simulation

1. Introduction

As city populations rise, traffic congestion, air pollution, and noise pollution become more prevalent. With their high capacity, quick speed, punctuality, convenience, and safety, metro systems have become a viable solution for relieving the pressure of surface traffic and solving typical urban development issues. The shield tunneling technique is widely employed among metro systems due to its benefits of highly safe construction efficiency, high automation, and low environmental effects [1–3]. The segmental lining of the shield tunnel is a vital component that sustains various loads, such as soil and water pressures. Prefabricated reinforced concrete segments and connecting bolts comprise the segmental lining. The tunnel ring has a symmetrical structure, usually comprising several standard segments, two special segments, and one key segment for metro shield tunnels.

The deformation properties and mechanical behavior of shield tunnels have been investigated in past decades through theoretical analysis, full-scale model tests, and numerical analysis. Various theoretical models have been proposed based on assumptions regarding the circumferential joints of the lining, mainly including the homogeneous circular model, the beam-spring model, and the shell-spring model. The homogeneous circular

model is an early, widespread analytical method. This approach is used in Japan to simplify the lining into a circular ring of homogeneous material, with joints in the lining considered by reducing the flexural stiffness of the ring [4–7]. Later, a beam-spring model was presented; it considered the mechanical behavior of joints instead of replacing segments and joints with beam elements and springs [8,9]. Furthermore, some researchers have proposed a shell-spring model to comprehensively simulate the mechanical properties of the segment; it employs elements units and springs to simulate segments and joints, respectively [10,11]. However, the theoretical analysis method has some limitations. On one hand, the three-dimensional characteristics of the segmental lining are relatively complicated. On the other hand, the analytical models simplify the segments and joints, making it virtually impossible to reflect their nonlinear mechanical characteristics.

Full-scale model tests are commonly used to investigate lining performance. These tests often use a loading system to load prototype tunnel rings. Many scholars have conducted full-scale model tests to investigate the lining structure's load-carrying capacities, deformation characteristics, and damage mechanisms [12–18]. Lu [18] conducted a full-scale model test on a segmental ring based on the Liyumen–Qianwan section of Shenzhen Metro Line 1, aiming to investigate the structure's mechanical response under a complex loading mode induced by adjacent constructions. The full-scale model test reflects the deformation characteristics and damage pattern of the lining more realistically, but it is too expensive and complicated. It becomes unaffordable to conduct many tests, making it difficult to generate rich data. Furthermore, the loading system simulates earth pressure by applying point or line loads. However, earth pressure acting on the lining is a continuous surface load. Hence, there are some differences between the two loading modes.

Compared to full-scale model tests, numerical analyses are more versatile in studying the mechanical behavior of lining under various working conditions and can generate more comprehensive and abundant data at a lower cost. The numerical simulation method has been employed to study the effects of complex conditions such as ground surcharge, excavation of the adjacent foundation pit, and shield tunneling undercrossing the existing shield tunnel [19–24]. Currently, the numerical simulation method simplifies the lining by modeling it as a homogeneous ring or simulating the joints with linear springs. With the effects of reinforcement ignored, none of these methods can accurately reflect the mechanical behavior of the joint. In the current research on shield tunnels, the changes of internal force are mainly focused on, while the deformation characteristics of the lining are less studied. Therefore, it is necessary to establish an improved model to study the lining performance that considers the frictional effects of reinforcement, bolts, and the segment interface.

In this study, we first propose an approach for the refinement modeling of shield tunnel lining. We establish a refined numerical model for the lining of a shield tunnel using finite element software containing detailed models of reinforcement and connecting bolts. In addition, we validate the model parameters using a full-scale model test. Based on this numerical model, we also investigate the deformation characteristics of the lining under different loading conditions. The convergence, joint opening, bolt stress, and reinforcement stress of the segmental lining are systematically analyzed. Meanwhile, we discuss the relationships between convergence and joint opening, bolt stress and joint opening. We also reveal the deformation characteristics of the segmental lining.

2. Numerical Model Construction and Validation

2.1. Finite Element Model

The typical segmental lining performance is based on the Shenzhen Metro tunnel. The outer diameter of the tunnel ring is 6000 mm, and the thickness and width of the segments are 300 and 1500 mm, respectively. A tunnel ring consists of three standard segments (B1, B2, and B3), two special segments (L1 and L2), and one key segment (F). Their central angles are 15°, 64.5°, and 72°, respectively. The tunnel ring is considered a symmetrical structure, as shown in Figure 1. Two bent bolts were used to connect the joints between

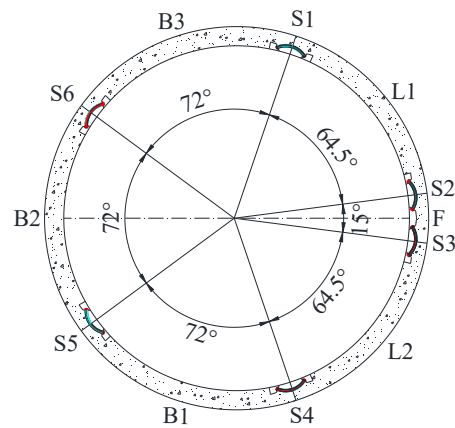the neighboring segments. The prestressed bent bolt nut and screw are 36 and 24 mm in diameter, respectively.

Figure 1. The geometry of the typical segmental lining.

Figure 2 shows a refined finite element model that includes precast concrete segments, bent bolts, bolt washers, bolt sleeves, and segment reinforcement. The number and distribution of rebars were consistent with the actual precast concrete segment configuration. The construction of the joints was simplified, and the effects of force transfer pads and waterproofing seal grooves at the joints were not considered. C3D8R elements were adopted for the concrete segments, bolts, bolt washers, and bolt sleeves, whereas T3D3 elements were used for the segment reinforcements.
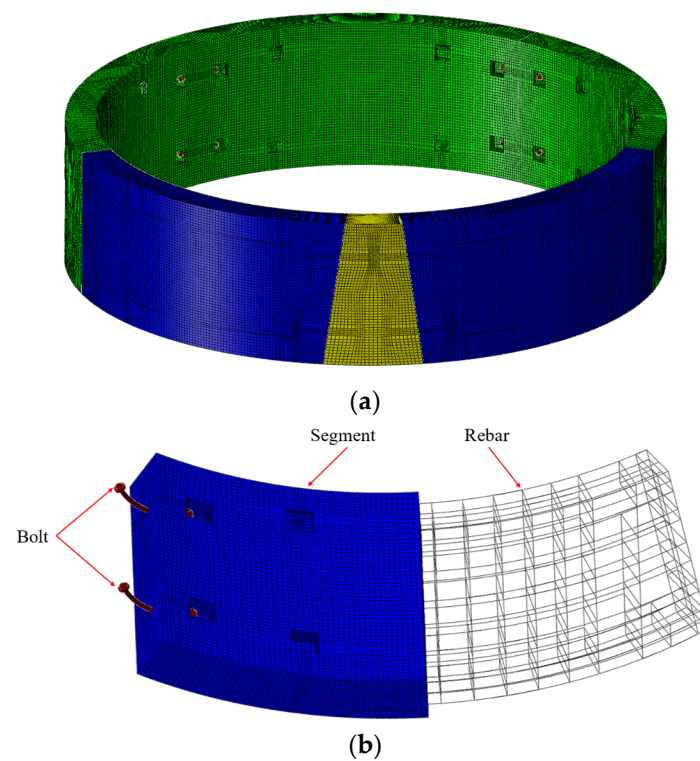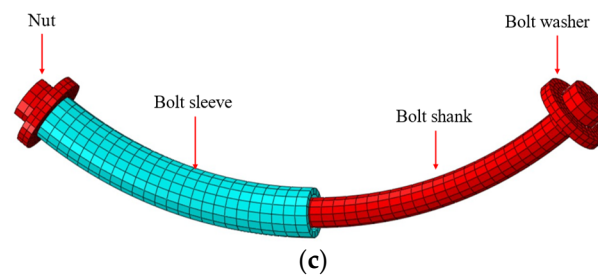

(**a**)

(**b**)

Figure 2. *Cont.*

(c)

Figure 2. Finite element model: (**a**) full ring, (**b**) segment, (**c**) bolt.

2.2. Constitutive Model and Parameters

The concrete's strength class for the precast segments is C50, and an elastoplastic double broken-line model describes the mechanical behavior of concrete. The main mechanical parameters of concrete were determined based on the experiment [18] and the Code for Design of Concrete Structures (GB 50010—2010) [25]. The strength class of the steel is HRB400, with 400 and 500 MPa in yield and ultimate strength, respectively. The bent bolts comprised 8.8-class high-strength steel, 640 MPa in yield strength, and 800 MPa in ultimate strength. The detailed parameters of each material are shown in Table 1.

Table 1. The main mechanical parameters.

Material	E (MPa)	v	σ_0 (MPa)	σ_u (MPa)
Segmental lining	34,500	0.2	46	55
Rebar	200,000	0.3	400	500
Bolt	206,000	0.3	640	800
Bolt washer	206,000	0.3	—	—
Bolt sleeve	2000	0.35	—	—

Notes: E is Young's modulus; v is Poisson's ratio; σ_0 is critical stress; σ_u is peak stress.

2.3. Interactions

The surface-to-surface contact model was adopted to simulate interactions between the segments and between the bolts and bolt sleeves. Surface-to-surface contact interactions describe contact between two deformable surfaces or between a deformable surface and a rigid surface, which includes the definition of contact discretization option and tracking approaches. The most general tracking method is the finite slip tracking approach, which allows for the arbitrary relative separation, sliding, and rotation of the contacting surfaces. It is used when there is a relatively large sliding or rotation between two contact surfaces. Moreover, compared to node-to-surface discretization, surface-to-surface discretization can better tackle the problem of main surface nodes penetrating the secondary surface [26]. Therefore, we adopted the finite slip tracking approach and surface-to-surface discretization for this study. The penalty function and hard contact govern the tangential and normal mechanical properties, respectively. The friction coefficient between adjacent segments is 0.5; it is 0.3 between bolt and bolt sleeves. The maximum allowable elastic slip is 0.005 times the characteristic surface size. The embedded constraints simulate the interaction between the steel bars and concrete segments. Tie constraints are used for interactions between the nut and bolt washer, bolt washer and concrete, and bolt sleeve and concrete.

2.4. Validation

The full-scale model tests conducted by Lu [18] were employed to validate the reliability of the model used in the numerical analyses. In the full-scale test, the loads acting on the lining include 24 concentrated forces pointing to the circle's center, with a central angle interval of 15°. Three types of loads were used in the experiment: six P_1 loads, ten P_2 loads, and eight P_3 loads. The load pattern for the test is symmetrical, as shown in Figure 3a. The loading levels and the corresponding magnitudes are presented in Table 2. Each loading

point consists of two jacks and a matching loading beam that is 250 mm long, 300 mm wide, and 450 mm high, as shown in Figure 3b.
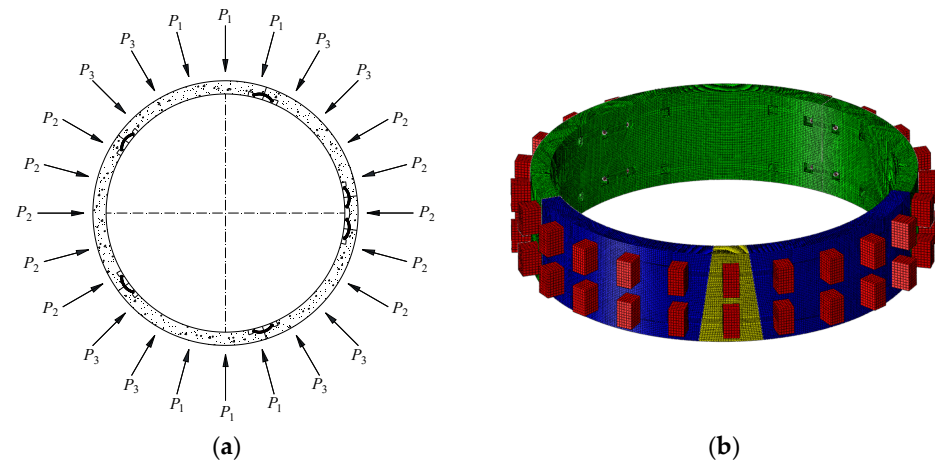

(**a**)   (**b**)

Figure 3. Schematic diagram of the loading on the ring in the full-scale model test: (**a**) schematic diagram of load distribution, (**b**) loading method of the numerical model.

Table 2. The loading procedure in the full-scale model test.

Level	P_1 (kN)	P_2 (kN)	P_3 (kN)	Level	P_1 (kN)	P_2 (kN)	P_3 (kN)
0	0	0	0	11	278	210	205
1	31	26.4	26.2	12	309.2	228	231
2	62	52.8	52.4	13	340.4	246	257
3	93	79.2	78.6	14	356	255	270
4	124	105.6	104.8	15	381.4	272.2	287.6
5	155	132	131	16	406.8	289.4	305
6	187	152.4	149.4	17	432.2	306.6	322.6
7	219	172.8	167.8	18	457.6	323.8	340
8	235	183	177	19	483	341	357.6
9	252.2	193.8	188.2	20	508.4	358.2	375
10	269.4	204.6	199.4	—	—	—	—

Figure 4 compares the results between the numerical analyses and the full-scale test, including horizontal convergence (Figure 4a) and the the joint opening at joint S5 (Figure 4b). Despite minor differences between the numerical and full-scale test results, the development trend of the ring deformation in the numerical simulation is consistent with the full-scale test. Therefore, numerical simulations representing the deformation and mechanical properties of the segmental lining are still highly justified.
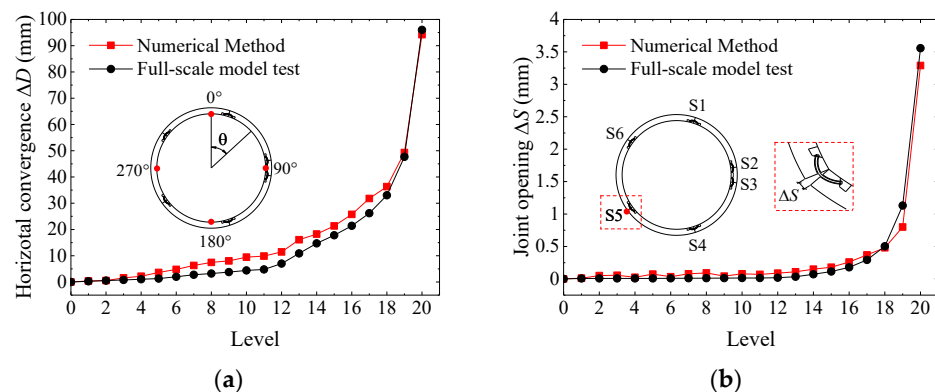

(**a**)   (**b**)

Figure 4. Comparison of results from the numerical analyses and the full-scale test: (**a**) horizontal convergence (**b**) joint opening.

3. Loading Mode and Numerical Cases

3.1. Loading Mode

In this study, we used the load-structure method to investigate the deformation characteristics of segmental lining under earth pressure. The loads mainly include vertical earth pressure, P_{v1}; horizontal earth pressure, P_x; the foundation reaction force, P_{y1}; and the self-weight of the segmental ring, G, where horizontal earth pressure is calculated by multiplying vertical earth pressure by the coefficient of lateral pressure λ. The horizontal earth pressure increases linearly with an increase in depth. The pressure distribution pattern around the tunnel is symmetrical, as shown in Figure 5a. A full circumferential ground spring was used to simulate the interaction of the soil and the segmental lining [27]. The resistance of the soil during tunnel deformation was simulated through the ground spring. Each node of the segmental lining surface element was constrained by three springs, one normal spring, and two shear springs, as shown in Figure 5b. The normal spring can be compressed but not pulled. Moreover, the stiffness of the normal spring was obtained by multiplying the coefficient of subgrade reaction k by the area of each element. The stiffness of the shear springs was one-third that of the normal springs, as suggested by Koyama [8] and Wang [28].
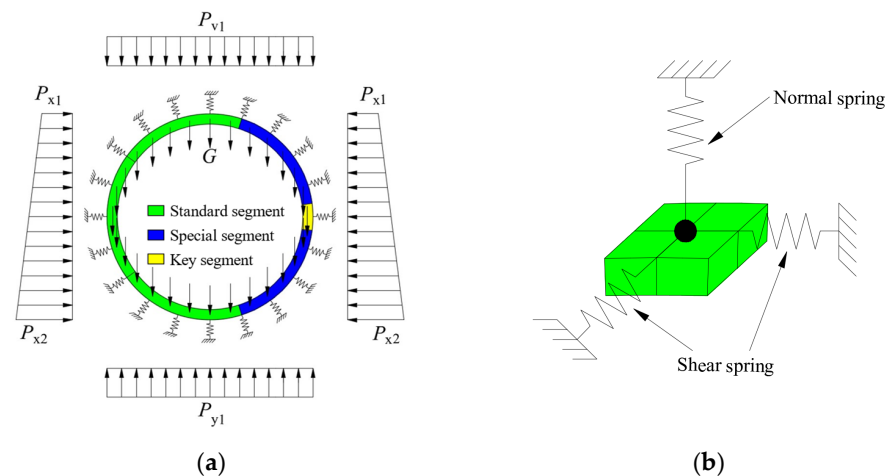

Figure 5. Calculation model of earth pressure around tunnel: (**a**) pressure distribution pattern around the tunnel, (**b**) ground spring.

3.2. Numerical Cases

Our study focuses on the deformation characteristics of the lining under different loading conditions. We only consider the effect of load variations on the lining in this study. Additionally, we consider applied load variations by varying the lateral pressure coefficient to achieve different earth pressure combinations. The vertical earth pressure ranges from 0 to 2000 kPa, and the horizontal earth pressure varies with vertical earth pressure. The specific working conditions are shown in Table 3.

Table 3. Summary of numerical cases.

Case	P_{v1} (kPa)	λ	k (kPa/m)
C1	0~2000	0.45	10,000
C2	0~2000	0.50	10,000
C3	0~2000	0.55	10,000
C4	0~2000	0.60	10,000
C5	0~2000	0.65	10,000

4. Results and Analyses

The segmental lining of a shield tunnel is assembled from several segments, and its deformation characteristics are different from a homogeneous ring. Due to the presence

of joints, the mechanical properties of the segmental lining are significantly reduced. We investigated the transverse deformation characteristics of the segmental lining in this study. Convergence, joint deformation, reinforcement stress, and bolt stress were systematically analyzed under different loading conditions.

4.1. Convergence

Figure 6a,b show the lining's vertical and horizontal displacement distribution, respectively (Case C1, P_{v1} = 2000 kPa). The tunnel ring has a "horizontal oval" pattern under earth pressure. The diameter is shortened vertically and elongated horizontally. The maximum vertical displacement of the lining is at joints S1 and S4 in Figure 6a,b. The maximum horizontal displacement is at the haunch. Figure 6c,d present the vertical and horizontal convergence variations with vertical earth pressure P_{v1}. In practical engineering, the amount of change in tunnel diameter is often used to represent the convergence of the tunnel, which is the most commonly used indicator for evaluating the overall deformation of the tunnel ring. Vertical convergence is the amount of change in diameter in the vertical direction, and horizontal convergence is the amount of change in diameter in the horizontal direction. A positive value of convergence indicates increased diameter, whereas a negative value indicates the reverse. As shown in Figure 6c,d, the vertical and horizontal convergences of the lining increase with the increase in vertical earth pressure under different loading conditions, and the convergences are parabolic with vertical earth pressure. The coefficient of lateral pressure determines the amount of horizontal earth pressure while restraining the deformation of the lining ring. Therefore, the greater the lateral pressure coefficient, the smaller the convergence. When the lateral pressure coefficient is 0.45 and the vertical earth pressure is 2000 kPa (Case C1), the vertical and horizontal convergences of the tunnel ring are −286.55 and 292.61 mm, respectively. When the lateral pressure coefficient is 0.65 and the vertical earth pressure is 2000 kPa (Case C5), the vertical and horizontal convergences of the tunnel ring are −115.53 and 120.13 mm, respectively. The horizontal convergence of the ring is larger than the vertical convergence.
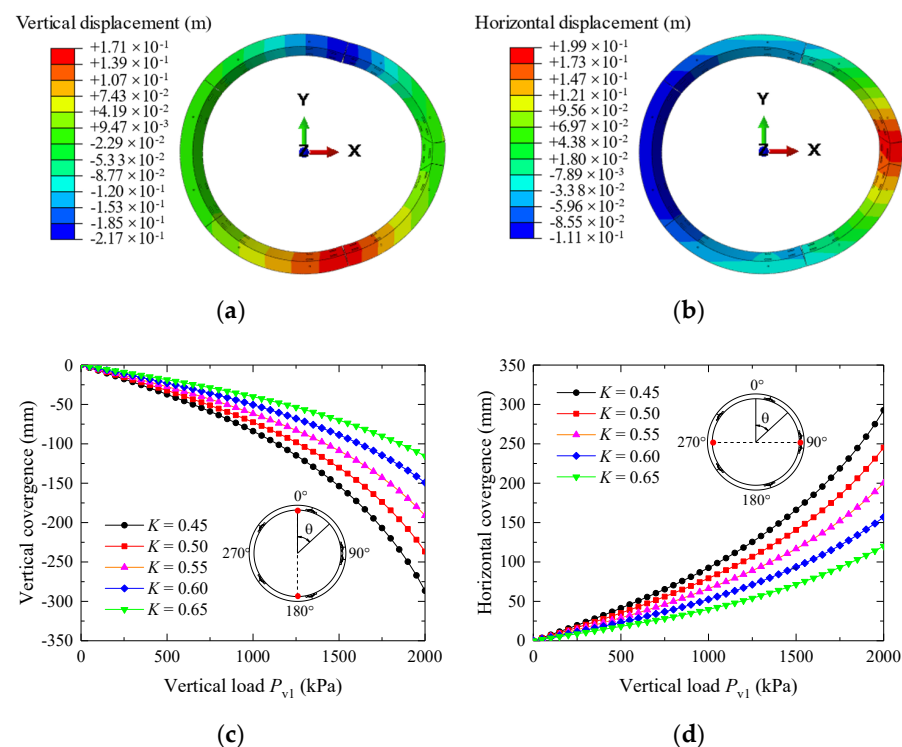

Figure 6. Displacement distribution and deformation of tunnel: (**a**) vertical displacement, (**b**) horizontal displacement, (**c**) vertical convergence, (**d**) horizontal convergence.

4.2. Joint Deformation

Figure 7a,b show the total and plastic strains of the concrete (Case C2, P_{v1} = 2000 kPa), respectively. Figure 7a indicates that a large tensile strain is distributed around the outer arc of the haunch and the inner arc of the crown and invert. The large compressive strain is distributed around the inner arc of the haunch and the joints. Figure 7b indicates that plastic deformation of the lining occurs at the joints. The concrete at the joint of the segment was squeezed under earth pressure, resulting in a large strain and the forming of a plastic hinge. The segment rotates around the plastic hinge, causing the joints to open. Joints S1 and S4 form a plastic hinge in the outer arc; therefore, the joints open in the inner arc, while joints S2, S3, S5, and S6 form a plastic hinge and open joints in the outer arc.
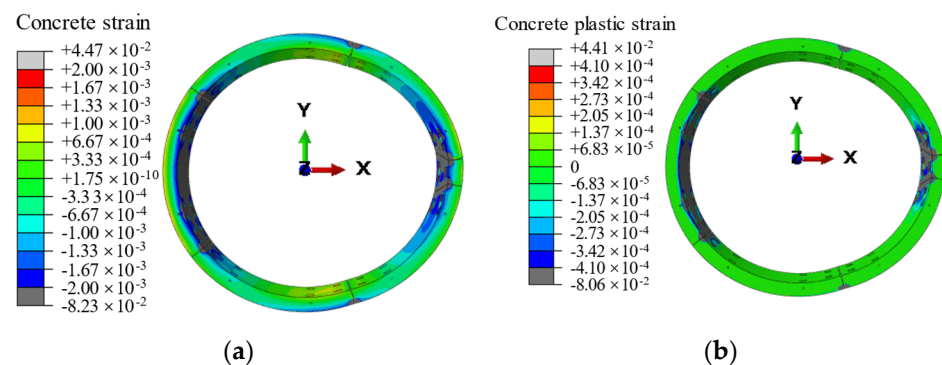

(a)   (b)

Figure 7. Strain distribution of the concrete: (**a**) total strain, (**b**) plastic strain.

Figure 8 shows the variation of joint openings. The amount of joint opening is an important indicator for evaluating the deformation of joints, and the deformation of joints is an important influencing factor of the water leakage of the joints; therefore, the amount of joint opening is commonly used to measure the leakage of joints in engineering. From Figure 8a,b,d–f, as vertical earth pressure increased, the opening of joints S1, S2, S4, S5, and S6 increased. The larger the coefficient of lateral pressure, the larger the joint opening. Segment L1 rotated counterclockwise around S2, and the outer arc of S2 opened. The greater the vertical earth pressure, the greater the rotation angle and joint opening. The same applies to the deformation of joints S1, S4, S5, and S6. As shown in Figure 8c, the joint opening of joint S3 first increased, then decreased. When the vertical soil pressure was low, the segment L2 rotated clockwise around S3. Therefore, the higher the vertical soil pressure, the larger the rotation angle. While segment F rotated less and moved to the right as a whole, the opening of joint S3 gradually increased. When vertical soil pressure was higher, segment F rotated around joint S3 due to the compression of segment L1, which reduced the opening of S3. Joints S1 and S2 had the most joint opening in the inner and outer arcs, respectively, under the same loading conditions. When the lateral pressure coefficient was 0.45, the joint opening of S1 and S2 were 34.64 and 28.54 mm, respectively. When the lateral pressure coefficient was 0.65, the joint opening was 9.70 and 7.84 mm, respectively.
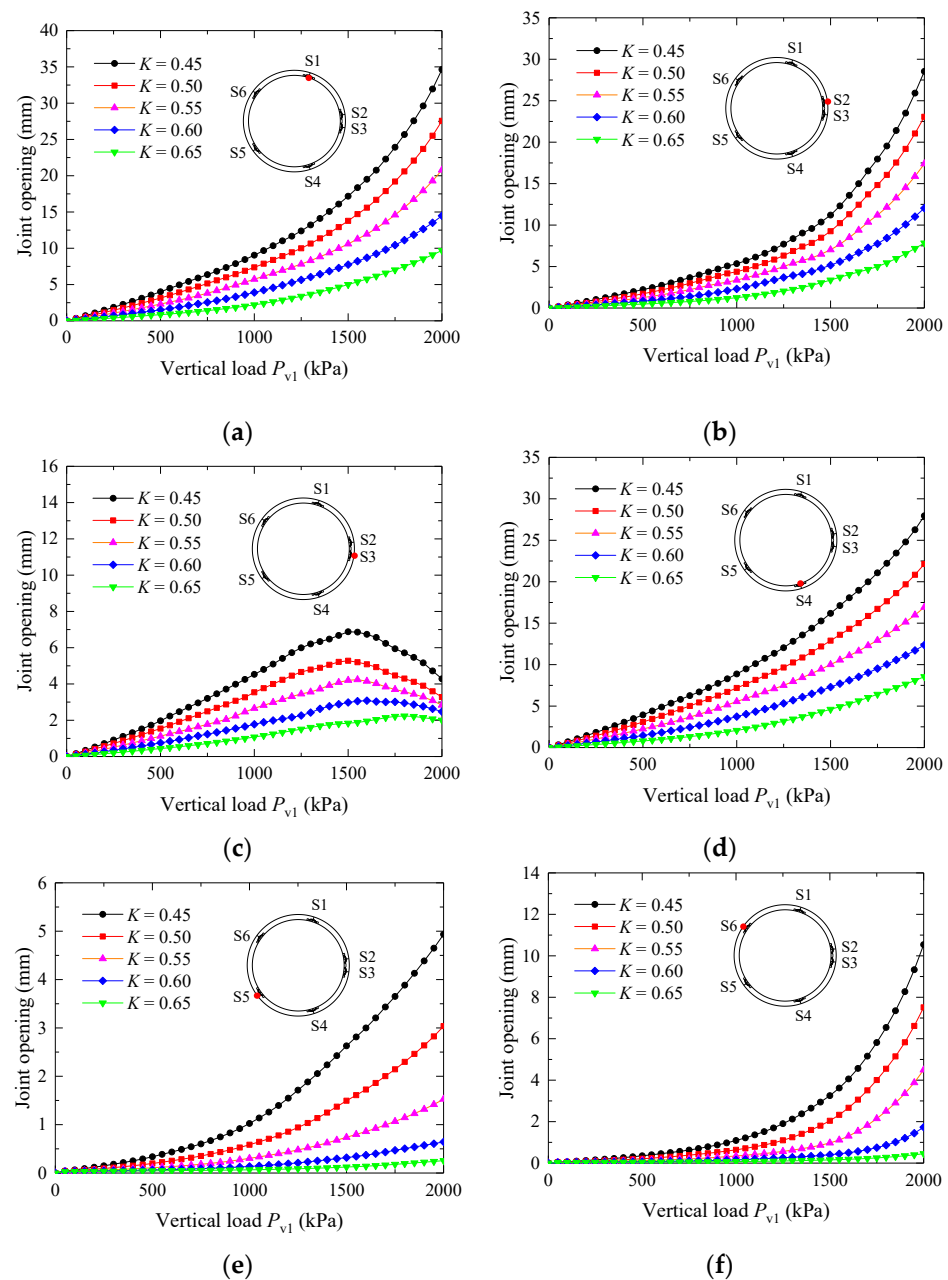
Figure 8. Variation of joint opening: (**a**) joint S1, (**b**) joint S2, (**c**) joint S3, (**d**) joint S4, (**e**) joint S5, (**f**) joint S6.

4.3. Rebar Stress

Rebar stress is an important indicator of the service condition of the segmental reinforcement. In this study, we have analyzed the distribution and variation of the stresses in the segmental reinforcement under different loading conditions. Figure 9 shows the stress distribution of the reinforcement (Cases C1 and C5, P_{v1} = 2000 kPa) and highlights the position of maximum tensile and compressive stresses in each segment. Figure 9a shows that the maximum tensile stress of each segment reinforcement is mainly distributed at the joint. The concrete at the segment joint is partially compressed under earth pressure, leading to the high tension of local reinforcement at the joint. The maximum compressive stress of each segment reinforcement is distributed near the joint and on the side of concrete compression. The main reason is that the segment rotates around the plastic hinge under earth pressure and the segments squeeze each other, leading to bending near the joint of the segment and greater rebar compression. Figure 9b also shows that the maximum tensile

stress of segment B2′s reinforcement is at the haunch; for the remaining segments, it is at the joints. When the deformation of the lining is small, the reinforcement stress caused by bending is greater than that caused by local extrusion.
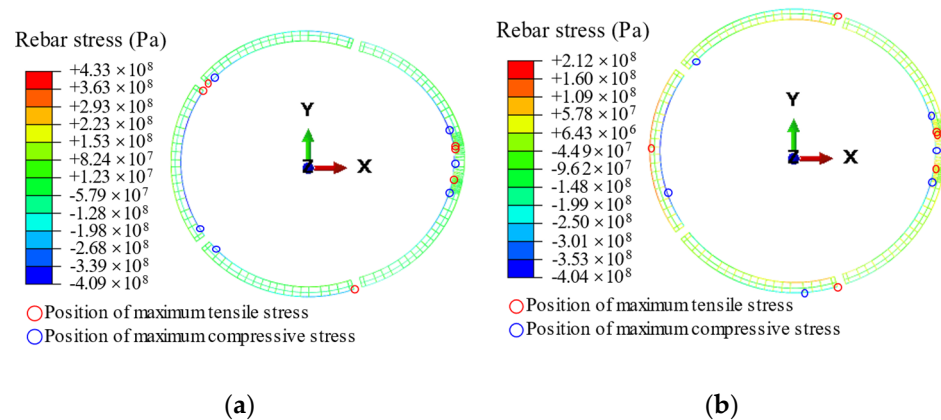

Figure 9. Distribution of rebar stress: (**a**) case C1, (**b**) case C5.

Figure 10 shows the variation of the tensile stress of the reinforcement. The maximum tensile stress point of the vertical earth pressure of 2000 kPa was measured to analyze the maximum tensile stress history of the reinforcement. Figure 10a,c,f show reinforcement stress variations in segments B1, B3, and L2, respectively. The development trend of reinforcement tensile stress is consistent. The reinforcement stress increases with an increase in vertical earth pressure and does not reach the yield strength of 400 MPa. Figure 10d,e show reinforcement stress variations in segments F and L1, respectively. The development of tensile stress is consistent under different loading conditions when vertical earth pressure is low. With increased vertical earth pressure, the development of tensile stress becomes different. The lateral pressure coefficient is lower, and the tensile stress is greater. Figure 10b shows the reinforcement stress variation in segment B2. The development of reinforcement stress in conditions with lateral pressure coefficients of 0.45, 0.50, 0.55, and 0.60 is inconsistent with conditions with a lateral pressure coefficient of 0.65. When the vertical earth pressure is 2000 kPa, the reinforcement stress of the lining shows different states under different loading conditions. When the lateral pressure coefficients are 0.45, 0.50, 0.55, and 0.60, the position of maximum stress is at the joint, whereas with the lateral pressure coefficient of 0.65, it is at the haunch. When the deformation of the lining is minor, the reinforcement stress at segment B2′s haunch is greater than that at the joint. Under the same loading conditions, the maximum tensile stress of the reinforcement is distributed to segment L1. The main reason is that joint S2 will greatly extrude during the deformation of the lining.
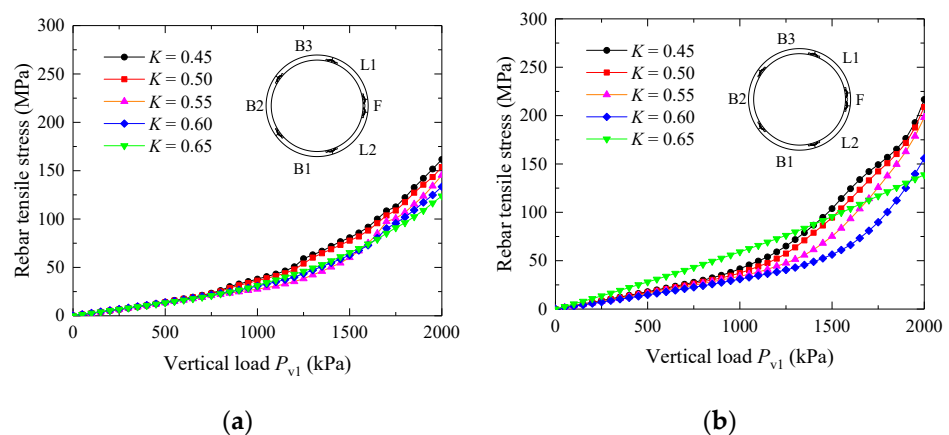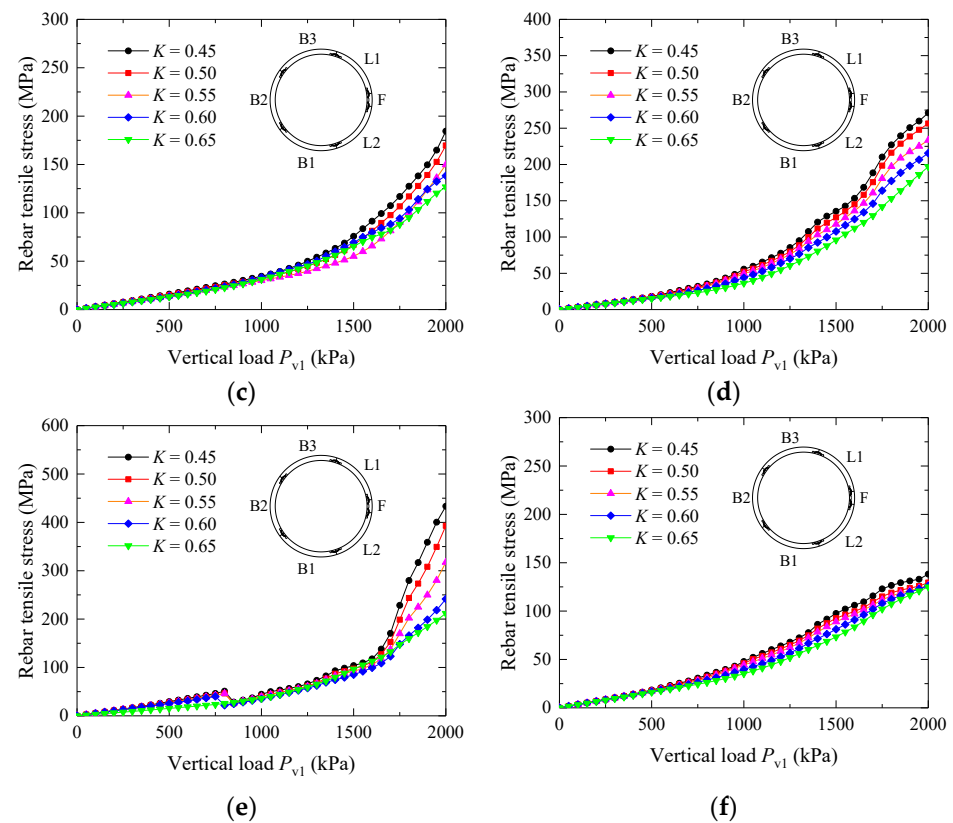

Figure 10. *Cont.*

Figure 10. Variation of rebar tensile stress: (**a**) segment B1, (**b**) segment B2, (**c**) segment B3, (**d**) segment F, (**e**) segment L1, (**f**) segment L2.

Figure 11 shows the variation in the compression stress of the reinforcement. Figure 11a–c show that the development of reinforcement tensile stress for segments B1, B2, and B3 under different loading conditions is consistent when vertical earth pressure is lower; however, with increased vertical earth pressure, the difference in reinforcement tensile stress becomes more significant. When the vertical earth pressure is 2000 kPa, the reinforcement stress of segment B2 reaches the yield stress of 400 MPa. Figure 11d–f show the compressive rebar stress of segments F, L1, and L2. The reinforcement stress of segments F, L1, and L2 remain the same under different loading conditions, which increase with an increase in vertical earth pressure.

4.4. Bolt Stress

Bolt stress is an important indicator of the service condition of joint connection bolts. In this study, we have analyzed the distribution and variation of the stresses in the joint connection bolts under different loading conditions. Figure 12a shows the stress distribution in the bolts (Cases C1 and C5, P_{v1} = 2000 kPa). Joints S1 and S4 have inner arc opening deformations, and the bolt is subjected to tension on the inner side and compression on the outer side. Figure 12a shows that the bolts at joints S1 and S4 have obvious deformation and high bolt stress. Figure 12a,b show a greater stress distribution in the middle and ends of the bolt when the joints are inner arc openings. The deformation of joints S2, S3, S5, and S6 are outer arc openings, and the bolt is subjected to outer tension and inner compression, among which joint S2′s opening is the largest. Figure 12a shows a greater stress distribution in the middle of the bolt when the outer arc surface of the joint opens.
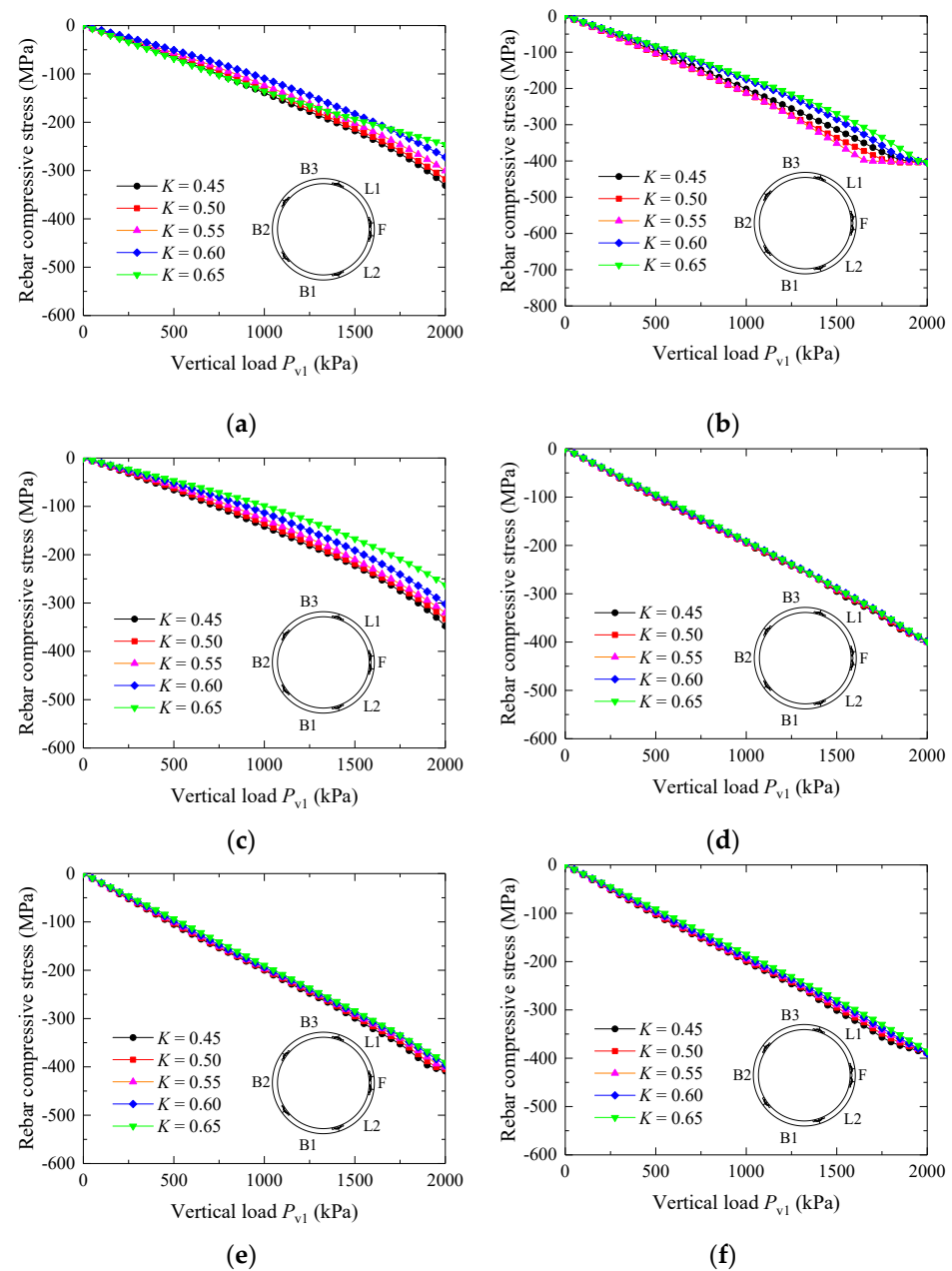
Figure 11. Variation of rebar compressive stress: (**a**) segment B1, (**b**) segment B2, (**c**) segment B3, (**d**) segment F, (**e**) segment L1, (**f**) segment L2.
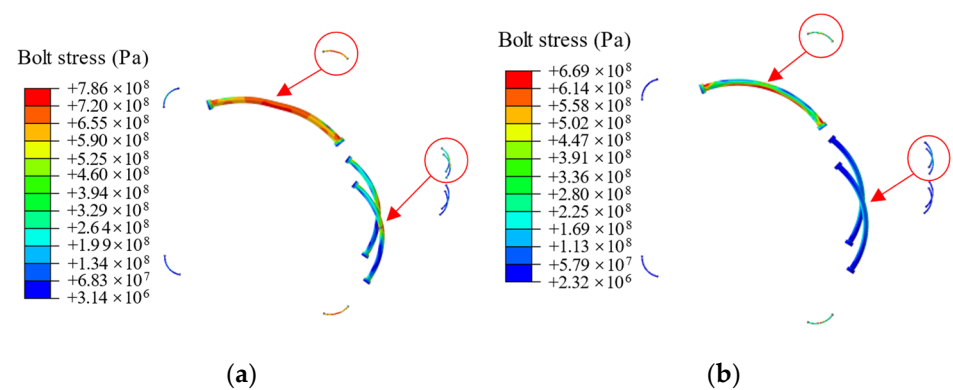

Figure 12. Distribution of bolt stress: (**a**) case C1, (**b**) case C5.

Figure 13 shows the bolt stress variation. A historical analysis of maximum bolt stress had a maximum stress point of 2000 kPa vertical earth pressure. Figure 13a,d show bolt stress variation at joints S1 and S4. The bolts gradually increase with an increase in vertical earth pressure and begin to stabilize after reaching the yield stress of 640 MPa. Before the bolt stress reaches the yield stress, it increases linearly with vertical earth pressure. When the lateral pressure coefficient is different, the vertical earth pressure of bolt stress reaching yield stress is also different. The greater the lateral pressure coefficient, the higher the vertical earth pressure of bolt stress reaching yield stress. Figure 13b shows the bolt stress variation at joint S2. The bolt stress reaches the yield stress when the lateral pressure coefficients are 0.45, 0.50, and 0.55. The bolt stress does not yield when the lateral pressure coefficients are 0.60 and 0.65. When the vertical earth pressure is <1400 kPa, the development of bolt stress is consistent. With the increase in vertical earth pressure, bolt stress gradually increases at different growth rates. The lower the lateral pressure coefficient, the faster the growth rate, and the lower the vertical earth pressure of bolt stress reaching the yield stress. Figure 13c,e,f show the bolt stress variation at joints S3, S5, and S6. The bolt stress at joints S3, S5, and S6 does not reach the yield stress. When the vertical earth pressure is low, there is little difference in the development of bolt stress. However, with an increase in vertical earth pressure, the difference in bolt stress development is more apparent.
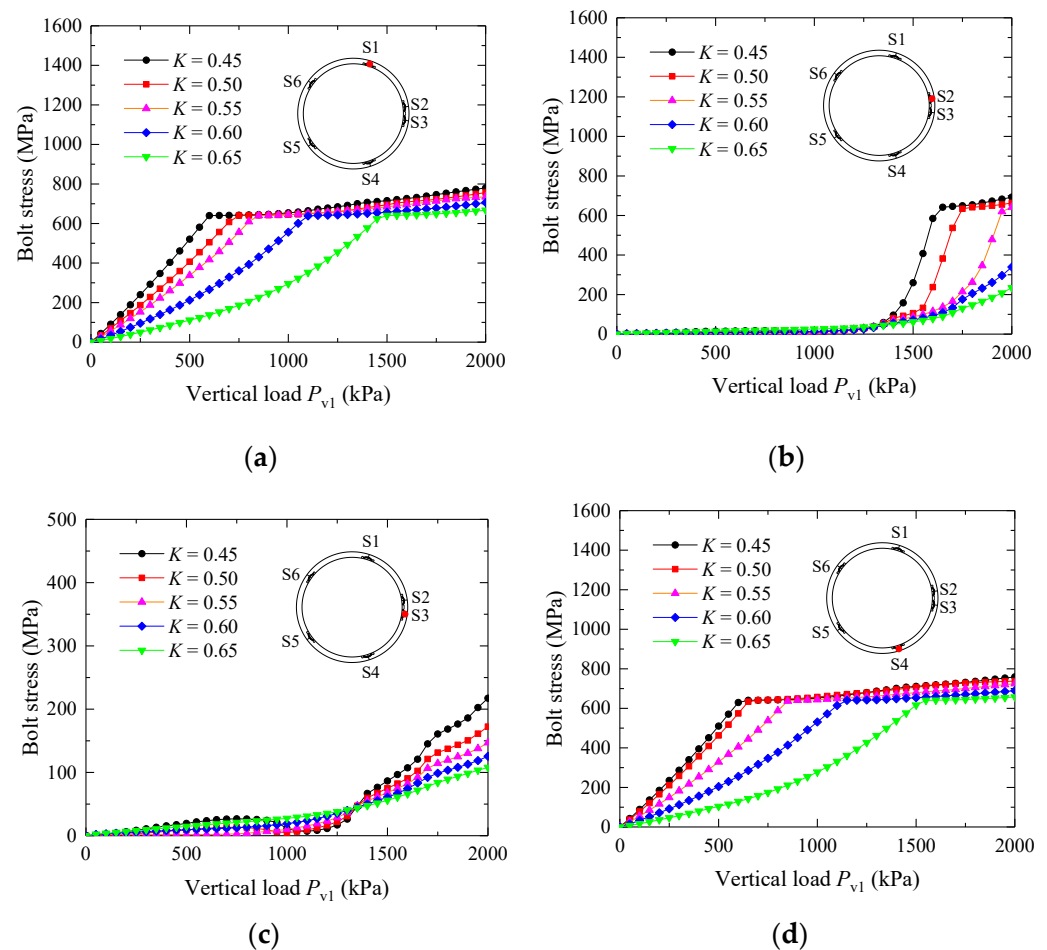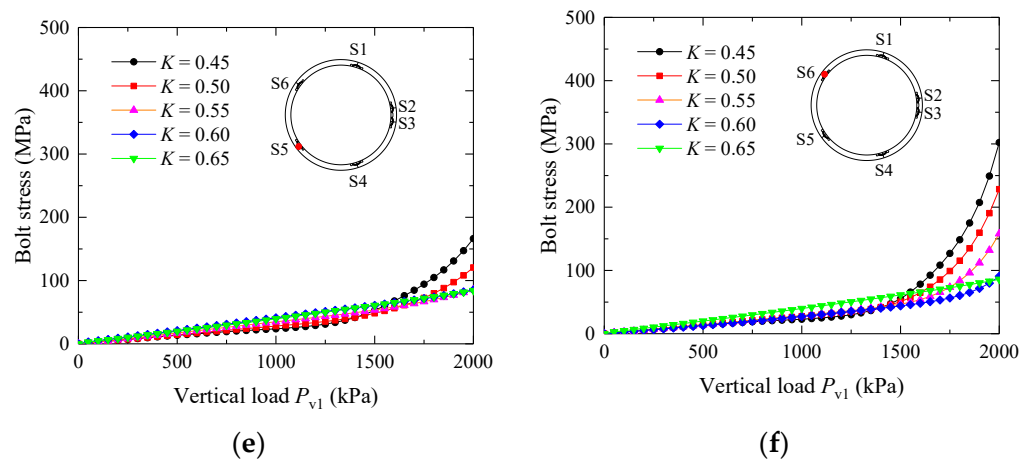

(a)

(b)

(c)

(d)

Figure 13. *Cont.*

Figure 13. Variation of bolt stress: (**a**) joint S1, (**b**) joint S2, (**c**) joint S3, (**d**) joint S4, (**e**) joint S5, (**f**) joint S6.

5. Discussions

The segment, and connecting bolts in the segmental lining work together to bear the external load. Previous research has considered the weakening effect of the joints on stiffness by discounting segments' stiffness or simplifying the joints as a series of springs. The joint is the weak point of the tunnel ring and it is necessary to discuss the relationship between the deformation of tunnel ring and the deformation of joint. Therefore, the relationships between convergence and joint opening and between joint opening and bolt stress are discussed in this study.

5.1. Relationship between Convergence and Joint Opening

The plastic hinge rotation of the segment around the joints mainly caused the deformation of the segmental lining. Therefore, the convergence of the segmental lining is closely related to the amount of joint opening. Figure 14 shows the relationship between horizontal convergence and joint opening. Figure 14a,d show the relationship between horizontal convergence and the joint opening of S1 and S4, respectively. The deformation of joints S1 and S4 are inner arc openings. The relationship between horizontal convergence and the joint openings of S1 and S4 is consistent under different loading conditions, and there is a linear relationship between them. Figure 14b,c,e,f show the relationship between horizontal convergence and joint opening amounts for S2, S3, S5, and S6, respectively. S2, S3, S5, and S6 are outer arc opening deformations. Figure 14b shows that the relationship between horizontal convergence and joint opening of S2 is consistent under different loading conditions, and there is a linear relationship between them. Figure 14c,e,f show that the relationships between the horizontal convergence and joint openings of S3, S5, and S6 are different. Under different loading conditions, the relationship between horizontal convergence and joint opening for S1, S2, and S4 is consistent, with a good linear relationship, whereas the relationship between the horizontal convergence and joint openings for S3, S5, and S6 is different. Horizontal convergence is a single index reflecting the deformation of the tunnel ring; it represents the overall deformation of the ring to a certain extent but not the deformation characteristics of the joint.
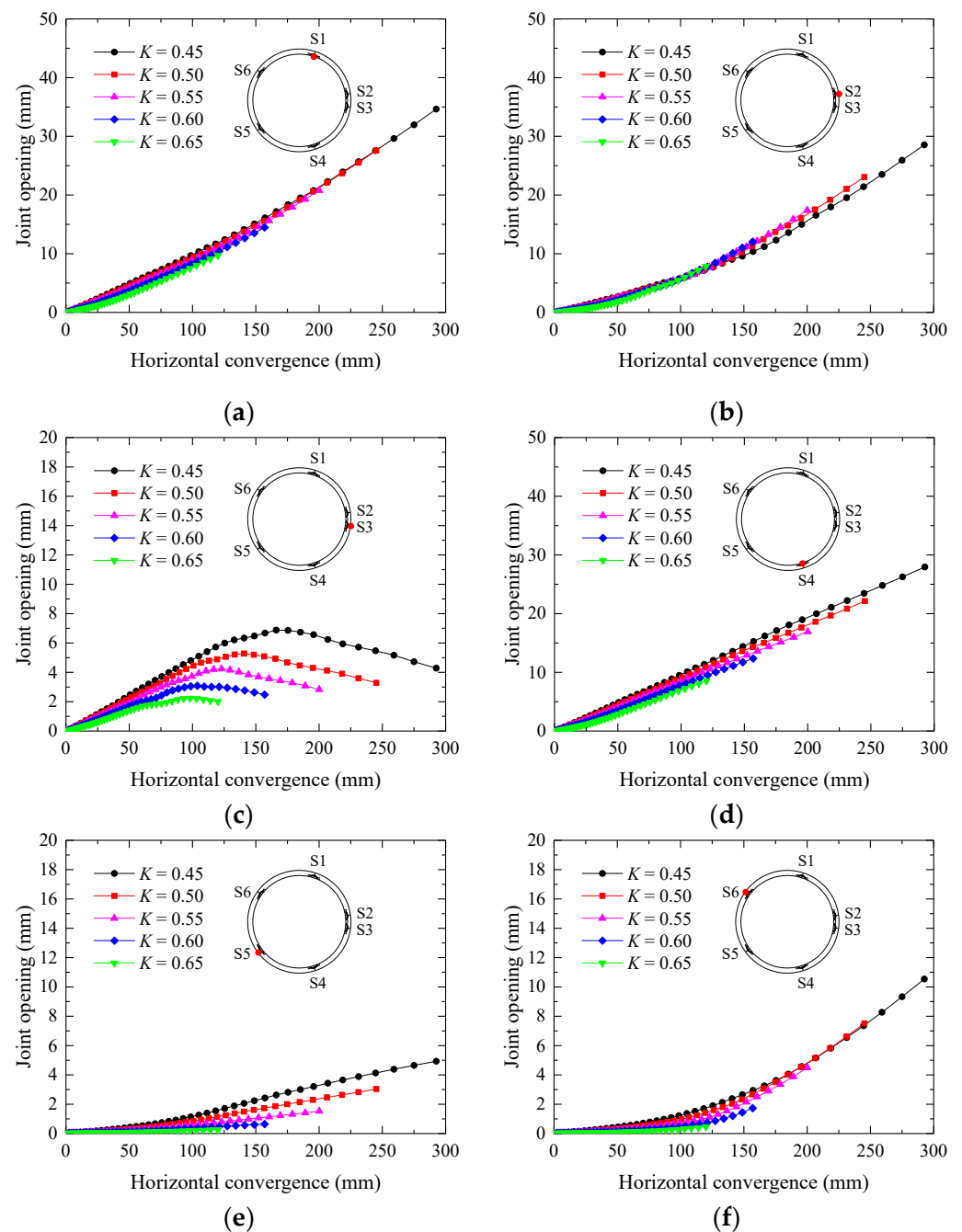
Figure 14. The variation of joint opening with the horizontal convergence: (**a**) joint S1, (**b**) joint S2, (**c**) joint S3, (**d**) joint S4, (**e**) joint S5, (**f**) joint S6.

5.2. Relationship between Joint Opening and Bolt Stress

Figure 15 shows the relationship between joint opening and bolt stress. In Figure 15a,d, the relationship between the joint opening and bolt stress in S1 is consistent, and that of S4 is the same. Before the bolt stress reaches the yield stress, the relationship between the joint opening amount and bolt stress increases linearly; then, it gradually becomes stable. When the lateral pressure coefficients are 0.45, 0.50, 0.55, 0.60, and 0.65, the bolt stress at joint S1 reaches the yield stress, with a joint opening of 5.43, 5.15, 4.54, 4.91, and 5.00 mm, respectively. The joint openings of S4 are 5.35, 4.61, 4.75, 4.64, and 4.92, respectively. When the joint is open in the inner arc, the bolt stress reaches the yield stress of 640 MPa, with a joint opening range of 4.50–5.50 mm. Figure 15b,c,e,f show the relationship between the joint opening amount and bolt stress of joints S2, S3, S5, and S6, respectively; the joint is

open in the outer arc. Joints S2, S3, S5, and S6 differ between joint opening and bolt stress. Figure 15b shows that the bolt stress at S2 reaches the yield stress with the joint openings of 5.43, 5.15, and 4.54 mm, when the lateral pressure coefficients are 0.45, 0.50, and 0.55. The bolt stress at S2 does not reach the yield stress when the lateral pressure coefficients are 0.60 and 0.65. Figure 14c,e,f show that the bolt stress at joints S3, S5, and S6 does not reach the yield stress, and the relationship between joint opening and bolt stress differs under different loading conditions. When the joint deformation is in the outer arc opening, the bolt stress is greatly affected by earth pressure. Under different loading conditions, the joint opening amount differs from the bolt stress. When the joint is open in the outer arc, the bolt stress reaches the yield stress, with a joint opening range of 14.00–17.50 mm.
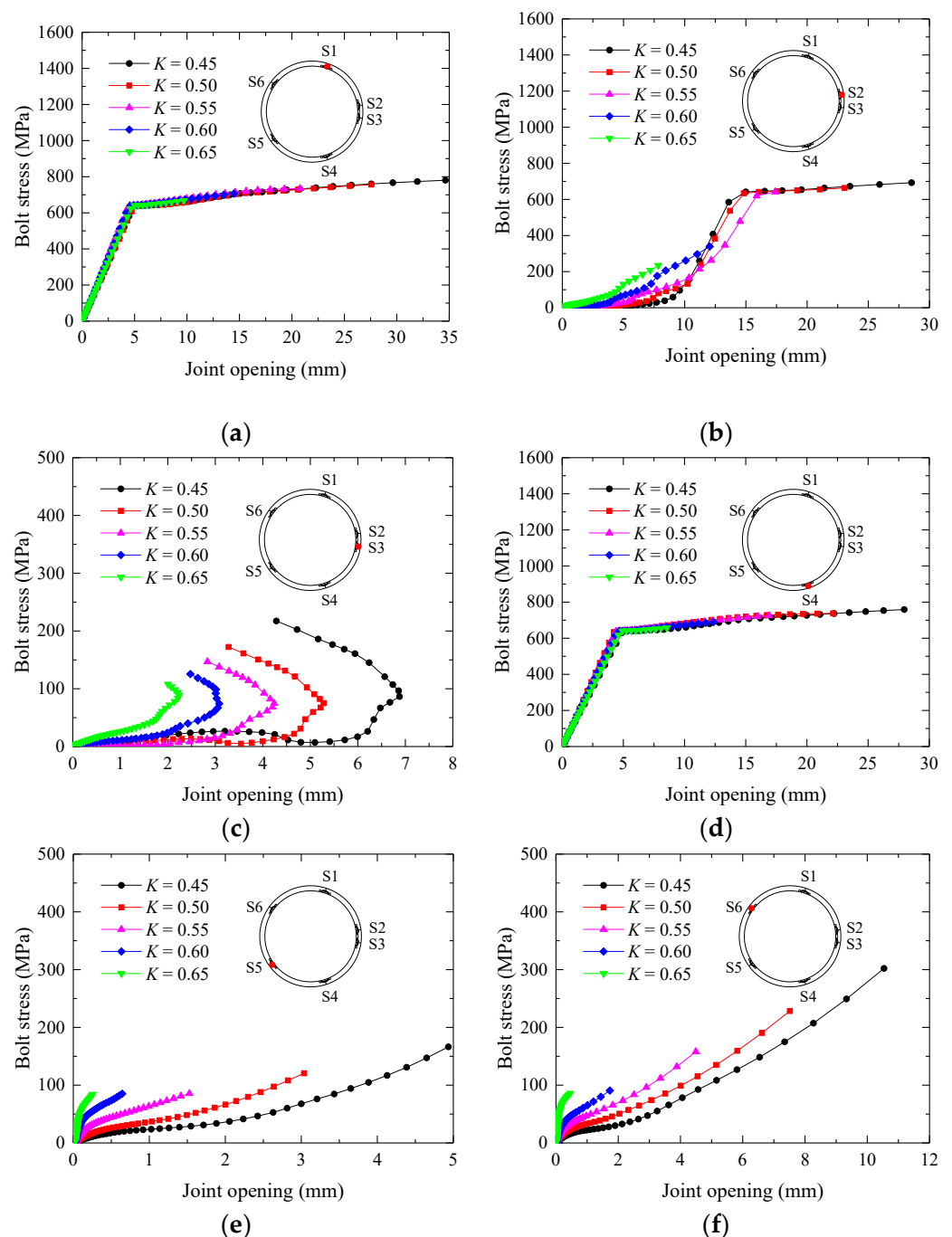

Figure 15. The variation of bolt stress with the joint opening: (**a**) joint S1, (**b**) joint S2, (**c**) joint S3, (**d**) joint S4, (**e**) joint S5, (**f**) joint S6.

6. Conclusions

In this study, we have developed a refined numerical model for segmental lining, incorporating reinforcement and joint bolts. We validated the parameters used in the model through the full-scale experimental results. Based on this numerical model, the deformation characteristics of the segmental lining were studied. Convergence, joint deformation, bolt stress, and reinforcement stress were systematically analyzed under different loading conditions. The deformation characteristics of the segmental lining were revealed. The conclusions of our study are as follows:

(1) In this study, we have established a refined numerical model for the segmental lining of a shield tunnel using finite element software, which contains detailed models of the reinforcement and connecting bolts. The model parameters were validated using a full-scale model test result. The numerical calculation results highly agree with the full-scale test, which verifies the accuracy of the numerical model. We prove that the refined numerical simulation method reasonably reflects the deformation of the segmental lining and can be used in subsequent studies.

(2) When the lining is deformed by earth pressure, the concrete at the joints is squeezed to produce large strains, resulting in plastic hinges forming at the joints. When the lining is deformed by earth pressure, the segment rotates around the plastic hinge, causing the joints to open. The rotation of the segment is the main reason for segmental lining deformation under earth pressure.

(3) Horizontal convergence is a single index reflecting the deformation of the tunnel ring, representing the overall deformation of the ring to a certain extent but not the deformation characteristics of the joint. When loading conditions differ, the relationship between joint opening and horizontal convergence is consistent for some joints and inconsistent for others.

(4) When the joint is open in the outer arc, the relationship between joint opening and bolt stress is different under different loading conditions. However, the relationship between joint opening and bolt stress is consistent when opening in the inner arc; bolt stress reaches a yield of 640 MPa, with a joint opening range of 4.50–5.50 mm.

Institutional Review Board Statement: Not applicable.

Informed Consent Statement: Not applicable.

Data Availability Statement: Not applicable.

Conflicts of Interest: The authors declare no conflict of interest.

References

1. Shen, S.L.; Cui, Q.L.; Ho, E.C.; Xu, Y.S. Ground response to multiple parallel Micro tunneling operations in cemented silty clay and sand. *J. Geotech. Geoenviron. Eng.* **2016**, *142*, 04016001. [CrossRef]
2. Wu, H.N.; Shen, S.L.; Yang, J.; Zhou, A.N. Soil-tunnel interaction modeling for shield tunnels considering shearing dislocation in longitudinal joints. *Tunn. Undergr. Space Technol.* **2018**, *78*, 168–177. [CrossRef]
3. Lei, M.F.; Peng, L.M.; Shi, C.H. An experimental study on durability of shield segments under load and chloride environment coupling effect. *Tunn. Undergr. Space Technol.* **2014**, *42*, 15–24. [CrossRef]
4. Wood, A. The circular tunnel in elastic ground. *Géotechnique* **1975**, *25*, 115–127. [CrossRef]

5.	Lee, K.M.; Ge, X.W. The equivalence of a jointed shield-driven tunnel lining to a continuous ring structure. *Can. Geotech. J.* **2001**, *38*, 461–483. [CrossRef]

6.	Liao, S.M.; Peng, F.L.; Shen, S.L. Analysis of shearing effect on tunnel induced by load transfer along longitudinal direction. *Tunn. Undergr. Space Technol.* **2008**, *23*, 421–430. [CrossRef]

7.	Huang, X.; Huang, H.W.; Zhang, J. Flattening of jointed shield-driven tunnel induced by longitudinal differential settlements. *Tunn. Undergr. Space Technol.* **2012**, *31*, 20–32. [CrossRef]

8.	Koyama, Y. Present status and technology of shield tunneling method in Japan. *Tunn. Undergr. Space Technol.* **2003**, *18*, 145–149. [CrossRef]

9.	Huang, W.M.; Wang, J.C.; Yang, Z.X.; Xu, R.Q. Analytical model for segmental tunnel lining with nonlinear joints. *Tunn. Undergr. Space Technol.* **2021**, *114*, 103994. [CrossRef]

10.	Huang, Z.R.; Zhu, W.; Liang, J.H.; Lin, J.; Jia, R. Three-dimensional numerical modelling of shield tunnel lining. *Tunn. Undergr. Space Technol.* **2006**, *21*, 434. [CrossRef]

11.	Arnau, O.; Molins, C. Three dimensional structural response of segmental tunnel linings. *Eng. Struct.* **2012**, *44*, 210–221. [CrossRef]

12.	Blom, C.; Van, D.; Jovanovic, P.S. Three-dimensional structural analyses of the shield-driven "Green Heart" tunnel of the high-speed line South. *Tunn. Undergr. Space Technol.* **1999**, *14*, 217–224. [CrossRef]

13.	Schreyer, J.; Winselmann, D. Suitability tests for the lining of the 4th Elbe tunnel tube–results of large-scale tests. *Tunnel* **2000**, *1*, 34–44.

14.	Vervuurt, A.; Luttikholt, A. Failure behavior of segmented tunnel linings: Numerical modeling validated by full scale tests. In Proceedings of the Eccomas Thematic Conference on Computational Methods in Tunneling, Vienna, Austria, 27–29 August 2007; pp. 1–13.

15.	Liu, X.; Dong, Z.; Bai, Y.; Zhu, Y.H. Investigation of the structural effect induced by stagger joints in segmental tunnel linings: First results from full-scale ring tests. *Tunn. Undergr. Space Technol.* **2017**, *66*, 1–18. [CrossRef]

16.	Liu, X.; Ye, Y.; Liu, Z.; Liu, Z.; Huang, D.Z. Mechanical behavior of Quasi-rectangular segmental tunnel linings: First results from full-scale ring tests. *Tunn. Undergr. Space Technol.* **2018**, *71*, 440–453. [CrossRef]

17.	Molins, C.; & Arnau, O. Experimental and analytical study of the structural response of segmental tunnel linings based on an in situ loading test. Part 1: Test configuration and execution. *Tunn. Undergr. Space Technol.* **2011**, *26*, 764–777. [CrossRef]

18.	Lu, Y. *Full-scale Model Test of Shield Tunnel Segment and Simulation Analysis of Circumferential Joint*; China Academy of Railway Sciences: Beijing, China, 2019. (In Chinese)

19.	Yamamoto, K.; Lyamin, A.V.; Wilson, D.W.; Sloan, S.W.; Abbo, A.J. Stability of a circular tunnel in cohesive-frictional soil subjected to surcharge loading. *Comput. Geotech.* **2011**, *38*, 504–514. [CrossRef]

20.	Liu, J.W.; Shi, C.H.; Lei, M.F.; Wang, Z.X.; Cao, C.Y. A study on damage mechanism modelling of shield tunnel under unloading based on damage–plasticity model of concrete. *Eng. Fail. Anal.* **2021**, *123*, 105261. [CrossRef]

21.	Shi, C.H.; Cao, C.Y.; Lei, M.F.; Peng, L.M.; Ai, H.J. Effects of lateral unloading on the mechanical and deformation performance of shield tunnel segment joints. *Tunn. Undergr. Space Technol.* **2016**, *51*, 175–188. [CrossRef]

22.	Jiang, L.; Hao, S.Y. Resilience Evaluation of the Existing Shield Tunnel Lining Induced by the Symmetrical Excavation of Adjacent Foundation Pit Based on Numerical Simulations. *Symmetry* **2022**, *14*, 229. [CrossRef]

23.	Lou, P.; Li, Y.H.; Lu, S.D.; Xiao, H.B.; Zhang, Z.G. Deformation and Mechanical Characteristics of Existing Foundation Pit and Tunnel Itself Caused by Shield Tunnel Undercrossing. *Symmetry* **2022**, *14*, 263. [CrossRef]

24.	Chakeri, H.; Hasanpour, R.; Hindistan, M.A.; Ünver, B. Analysis of interaction between tunnels in soft ground by 3D numerical modeling. *Bull. Eng. Geol. Environ.* **2011**, *70*, 439–448. [CrossRef]

25.	*GB50010*; Code for Design of Concrete Structures. China Architecture and Building Press: Beijing, China, 2010. (In Chinese)

26.	ABAQUS. *Abaqus User's Manual, Version 2021*; Hibbit, Karlsson & Sorenson, Inc.: Pawtucket, RI, USA, 2021.

27.	Mashimo, H.; Ishimura, T. Evaluation of the load on shield tunnel lining in gravel. *Tunn. Undergr. Space Technol.* **2003**, *18*, 233–241. [CrossRef]

28.	Wang, F.; Zhang, D.M.; Zhu, H.H.; Huang, H.W.; Yin, J.H. Impact of overhead excavation on an existing shield tunnel: Field monitoring and a full 3D finite element analysis. *CMC—Comput. Mater. Con.* **2013**, *34*, 63–81.